ACS NANO
Cite This: ACS Nano 2019, 13, 10745−10753
www.acsnano.org

ARTICLE

Optical Constants and Effective-Medium Origins of Large Optical Anisotropies in Layered Hybrid Organic/Inorganic Perovskites

Ryan A. DeCrescent,[†] Naveen R. Venkatesan,[‡] Clayton J. Dahlman,[‡] Rhys M. Kennard,[‡] Michael L. Chabinyc,[‡] and Jon A. Schuller*[,¶]

[†]Department of Physics, University of California Santa Barbara, Santa Barbara, California 93106, United States
[‡]Department of Materials, University of California Santa Barbara, Santa Barbara, California 93106, United States
[¶]Department of Electrical and Computer Engineering, University of California Santa Barbara, Santa Barbara, California 93106, United States

Supporting Information

ABSTRACT: Hybrid organic/inorganic perovskites (HOIPs) are of great interest for optoelectronic applications due to their quality electronic and optical properties and the exceptional ease of room-temperature synthesis. Layered HOIP structures, *e.g.*, Ruddlesden−Popper phases, offer additional synthetic means to define self-assembling multiple quantum well structures. Measurements of Ruddlesden−Popper HOIP optical constants are currently lacking, but are critical for both a fundamental understanding as well as optoelectronic device design. Here, we use momentum-resolved optical techniques to measure error-constrained complex uniaxial optical constants of layered lead-iodide perovskites incorporating a variety of organic spacer molecules. We demonstrate how large optical anisotropies measured in these materials arise primarily from classical dielectric inhomogeneities rather than the two-dimensional nature of the electronic states. We subsequently show how variations among these materials can be understood within a classical effective-medium model that accounts for dielectric inhomogeneity. We find agreement between experimentally inferred dielectric properties and quantum-mechanical calculations only after accounting for these purely classical effects. This work provides a library of optical constants for this class of materials and clarifies the origins of large absorption and photoluminescence anisotropies witnessed in these and other layered nanomaterials.

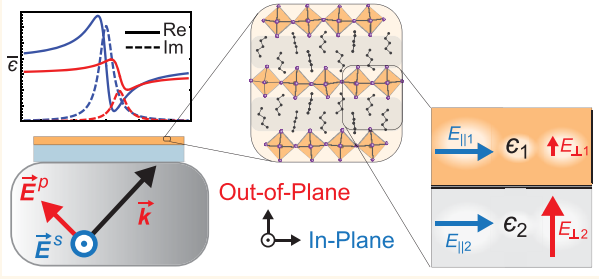

KEYWORDS: *2D materials, optical constants, momentum-resolved, electric dipoles, optical anisotropies, effective medium, hybrid perovskites*

When semiconductors are reduced to atomic length scales, unique optical properties emerge that reflect changes in both electronic structure and electromagnetic interactions.[1,2] This confinement often leads to enhanced light−matter interactions, making two-dimensional (2D) semiconductors promising and versatile materials for optoelectronics.[3−5] The burgeoning class of layered hybrid organic−inorganic perovskites (HOIPs), though not atomically thin *per se*, are also recognized as 2D materials since carriers are confined at the atomic scale within noninteracting semiconducting layers (*e.g.*, Figure 1a).[6−9] Facile synthesis by solution-processing methods,[10−13] outstanding optical properties,[6,14−17] and structural versatility[6,11,12] make 2D HOIPs attractive materials for optoelectronic and photonic applications.[12,18−22] The optical constants of 2D HOIPs have not yet been well characterized, despite being indispensable for fundamental understanding and development of optoelectronic devices.

Indeed, obtaining accurate optical constants is particularly challenging given the significant optical anisotropies common to 2D materials. Variable-angle spectroscopic ellipsometry (VASE; schematically illustrated in Figure 1b)—the canonical technique for characterizing thin-film optical constants[23,24]—provides Kramers−Kronig-consistent results over a broad wavelength range between the ultraviolet and mid-infrared. However, the need for *a priori* dispersion models, a large number of correlated free parameters, and low sensitivity to the out-of-plane optical response make the determination of

Received: July 14, 2019
Accepted: September 6, 2019
Published: September 6, 2019

DOI: 10.1021/acsnano.9b05504
ACS Nano 2019, 13, 10745−10753

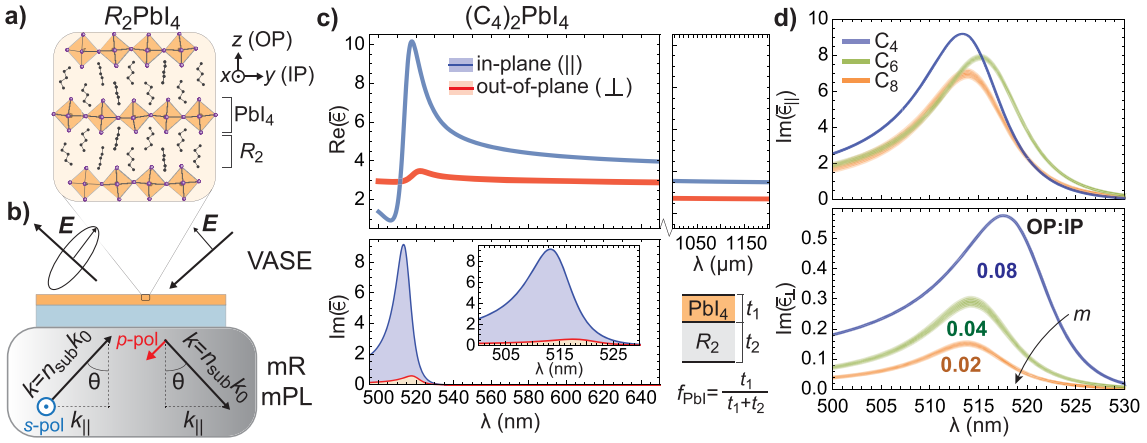

Figure 1. Quantifying variations in effective absorption anisotropies in $(C_m)_2PbI_4$ with m = 4, 6, and 8. (a) Schematic crystal structure of R_2PbI_4. (b) Complex uniaxial optical constants of spin-cast thin films are determined by a combination of momentum-resolved reflectometry (mR; from the substrate) and VASE (from the superstrate, ambient). Momentum-resolved PL (mPL) is used to measure PL anisotropies, also from within the substrate. (c) Complex uniaxial permittivity of $(C_4)_2PbI_4$ (butylammonium lead iodide). In-plane (||) components are shown in blue; out-of-plane (⊥) components are shown in red. Real components are shown in the upper panel; imaginary components are shown in the lower panel. The inset shows a magnified view of the imaginary components around the exciton absorption resonance. Schematic illustrates how the volumetric fill fraction of PbI_4 layers (f_{PbI}) depends on the length of the R cation (orange: PbI layers; gray: R bilayers). (d) Magnified view of (upper panel) IP components, Im($\bar{\epsilon}_{||}$), and (lower panel) OP components, Im($\bar{\epsilon}_{\perp}$), for films prepared with R = C_4 (blue), C_6 (green), and C_8 (orange). Approximate ratios of integrated OP:IP absorption strengths (Table 1) for each material are specified in the upper panel.

reliable optical constants *via* VASE an unsuspectingly difficult task.[25−27] In contrast, momentum-resolved spectroscopies offer unique advantages and have proven to be powerful techniques for quantifying optical constants and anisotropies in 2D semiconductors[28] and organic thin films.[29−31] For example, momentum-resolved reflectometry (mR; Figure 1b) provides well-conditioned optical constants *via* "turn-key" approaches that obviate modeling uncertainties inherent to VASE.[30,32]

Here, we use a self-consistent combination of mR and VASE to generate continuous Kramers−Kronig-consistent optical constants with reliable estimates of the optical anisotropies. We subsequently quantify absorption and photoluminescence (PL) anisotropies in various 2D HOIP thin films, which tend to adopt highly oriented structures with semiconducting lead-iodide layers parallel to the substrate interface (*e.g.*, Figure 1a; Supporting Information S1). Though the electronic structure and dielectric properties of the inorganic layer are known to be weakly sensitive to the choice of the organic cation, R (Figure 1a),[9,33,34] the thin-film optical response varies significantly between compounds.[6,35] We show how these variations arise primarily from classical electromagnetic effects—rather than quantum mechanical effects—owing to dielectric inhomogeneities inherent to this class of materials. We develop and present an effective-medium model that accounts for such effects and show how it can explain recent observations in other inhomogeneous nanomaterials, including CdSe nanoplatelets. These results provide critical optical characterizations useful for basic and applied studies of 2D HOIP optoelectronics and, more generally, establish the connection between experimentally measured optical anisotropies and quantum-mechanical calculations. Extensive details of our procedures and a complete set of optical constants for all samples studied here are presented in Supporting Information Sect. S2 (Figures S2 and S3) and are provided as supporting data.

RESULTS AND DISCUSSION

Quantifying Linear Absorption Properties. Figure 1c shows the in-plane (IP; blue) and out-of-plane (OP; red) complex permittivities, $\bar{\epsilon}_{||}$ and $\bar{\epsilon}_{\perp}$, respectively, of a butylammonium lead iodide ($(CH_3)(CH_2)_3NH_3)_2PbI_4$, henceforth $(C_4)_2PbI_4$) thin film (Figure 1a; Methods). The real and imaginary components are presented in the top and bottom panels, respectively. For the spin-cast thin films studied here, experiments observe averages over crystalline grains with different IP orientations. Therefore, these measurements cannot effectively distinguish between IP anisotropies that may exist in, for example, the material's orthorhombic phase. Nonetheless, these IP anisotropies are known to be very weak relative to the IP/OP anisotropy[6] and will henceforth be ignored. A sharp IP absorption peak, seen in Im($\bar{\epsilon}_{||}$), around 510 nm originates from the 1s exciton, which is confined to the PbI layers.[7,16,36] The maximum of the OP absorption, Im($\bar{\epsilon}_{\perp}$), is much smaller, approximately 1/10 that of Im($\bar{\epsilon}_{||}$). These results agree well with several early experimental investigations of single-crystal 2D HOIPs, which revealed a strong IP excitonic resonance with a very weak (approximately 5%) OP component.[6,36] This strong uniaxial response has generally been attributed to a 2D character of the exciton,[37] ultimately arising from a 2D electronic structure of the metal halide layers.[38] Associated with these absorption resonances are complementary variations in Re($\bar{\epsilon}_{||}$) and Re($\bar{\epsilon}_{\perp}$). This large absorption anisotropy produces a substantial birefringence, $\Delta n = n_e - n_0 = -0.731$, where $n_{o,e} = \sqrt{\bar{\epsilon}_{||,\perp}}$, just below the absorption onset, which settles to $\Delta n = -0.168$ in the infrared (right subpanel). Films prepared with phenethylammonium, ($C_6H_5(CH_2)_2NH_3$, henceforth PEA) (Figure S3), exhibit an even larger birefringence, $\Delta n = -0.836$.

Similar optical constants are measured for spin-cast films prepared with longer alkylammonium cations, R = (CH_3)-$(CH_2)_{m-1}NH_3$) (henceforth C_m) with m = 6 and 8 (Figure 1d; Figures S3 and S4). For increasing R cation length (*i.e.*,

DOI: 10.1021/acsnano.9b05504
ACS Nano 2019, 13, 10745−10753

increasing m), we find a subtle but systematic decrease in the IP absorption, Im($\bar{\epsilon}_{\parallel}$) (Figure 1d, top panel). Interestingly, Im($\bar{\epsilon}_{\perp}$) decreases much more rapidly as m is increased (Figure 1d; bottom panel). The ratio of the OP:IP absorption strengths, $|M_{IP}|^2/|M_{OP}|^2$ where $|M_{IP,OP}|^2 = \int \mathrm{Im}[\epsilon_{\parallel,\perp}(\lambda)]\, d\lambda$, consequently decreases from approximately 0.08 to 0.02 as m increases from 4 to 8. Similar trends in absorption anisotropies[6,35] and corresponding photoluminescence anisotropies[35] have been observed in previous studies, but the origins remain unresolved. Below, we show how these effects arise from classical local electric field inhomogeneities.

Quantifying Photoluminescence Properties. Momentum-resolved spectroscopies can also be used to resolve distinct IP and OP components of *emission* dipole moments. For example, momentum-resolved photoluminescence (mPL) has been used to quantify the orientation of individual molecules[39] and the average tilt angles of polymers in organic semiconducting thin films.[29] Recently, mPL has been used to quantify emission anisotropies in a variety of novel hybrid nanomaterials, including 2D HOIPs[35] and quantum-confined CdSe nanoplatelets embedded in an oleic acid matrix.[40] In both cases, large anisotropies inferred from the mPL analyses were directly attributed to anisotropies of the band-edge wave functions of the emissive layers (*e.g.*, CdSe in ref 40, semiconducting PbI monolayers in ref 35).

Experimental p-polarized momentum-resolved radiation patterns are shown in Figure 2a for (blue dots) m = 4, (orange dots) m = 6, and (green dots) m = 8 thin films of equivalent thickness (Methods and Figure S1). PL anisotropies are most evident near the critical angle of total internal reflection ($k_{\parallel} = k_0$; Figure 2b), the region into which OP (IP) dipoles radiate maximally (minimally); the larger the suppression of PL at $k_{\parallel} \approx k_0$, the larger the degree of anisotropy.[28] Consistent with the measured absorption anisotropies, this minimum becomes more pronounced as m increases from (blue) 4 to (green) 8, implying a decreasing OP dipole strength with increasing m. (See Supporting Information S3 for further discussion.)

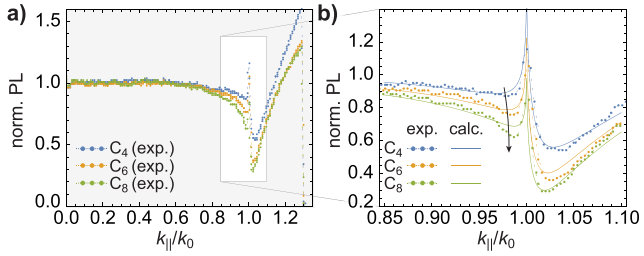

Figure 2. Quantifying variations in effective emission anisotropies in $(C_m)_2PbI_4$ with m = 4, 6, and 8. (a) Experimental (normalized) p-polarized momentum-resolved PL (mPL) from 43 nm thick films of $(C_m)_2PbI_4$ with (blue) m = 4, (orange) m = 6, and (green) m = 8. Data at each $k_{\parallel}$-point has been integrated in energy over the emission band. (b) Magnified view of the data shown in subpanel (a) around the critical angle of total internal reflection ($k_{\parallel}/k_0$). mPL counts in this region sensitively depend on both the OP emission dipole moment and the out-of-plane refractive index. Theoretical mPL counts (solid lines), calculated using optical constants for each material, demonstrate the excellent fit quality.

We quantify emission anisotropies by fitting the p-polarized radiation patterns to a combination of IP and OP dipoles, independently at each wavelength. Note, however, that this procedure requires accurate estimates of the anisotropic refractive index at the emission wavelengths, further motivating the need for the detailed measurements and analysis described above. Although the trend among materials (*vide infra*) is similar to that found in absorption, the ratios are uniformly smaller; OP:IP emission ratios in films prepared with C_4, C_6, and C_8 are found to range between ~0.01 (C_8) and 0.06 (C_4). In films prepared with PEA, the ratio is found to be 0.04. While some portion of this discrepancy may arise from compounded experimental errors between input optical constants (particularly the OP components) and measured radiation patterns, analyses on different samples return similar ratios. In general, however, emission and absorption anisotropies need not be equivalent, as they arise from fundamentally distinct optical processes. Later, as for absorption, we will explore these variations in the context of classical electric field inhomogeneities.

Table 1 summarizes optical parameters of the materials discussed here, including films with PEA R cations that have interlayer spacings comparable to C_6 films[10,41] (Figure S1) but a larger molecular polarizability.[33] Experimentally, we find a significantly larger OP optical response in films prepared with PEA (Table 1, Figures S3 and S4). At first sight, these large variations are surprising and appear to be inconsistent with quantum-mechanical calculations that suggest nearly invariant dielectric constants of the constituent layers.[33,34] We next show how these variations between different materials largely arise from classical electromagnetic effects that can be accounted for using an effective-medium model.

Deconvolving Classical and Quantum-Mechanical Anisotropies. The significant dielectric inhomogeneity inherent to 2D HOIPs sets them apart from conventional quantum-well systems composed of III–V semiconductors.[42] Consequently, anisotropies are expected to arise at a purely classical level. Indeed, Guo *et al.*[43] and Fieramosca *et al.*[35] acknowledged the analogy between 2D HOIPs and layered optical metamaterials.[44,45] However, no attempt has yet been made to deconvolve these *effective* anisotropies from anisotropies *intrinsic* to the constituent layers.

The significance of this inhomogeneity is easily understood within the context of first-order perturbation theory. The transition rate, Γ_{fi}, of an electric dipole, $\vec{M}_{fi}$, at position (x, y, z)

Table 1. Structural and Optical Parameters for Spin-Cast Thin Films Prepared with Various R Cations[a]

R cation	f_{PbI} (c-axis spacing)	norm. IP osc. strength ($\lvert M_{IP}\rvert^2$)	norm. OP osc. strength ($\lvert M_{OP}\rvert^2$)	OP:IP strength ratio	$\epsilon_{\perp,\infty}$	$n_e - n_0$ (λ = 530 nm) [$n_e - n_0$ (λ = 1000 nm)]
C_4	0.462 (13.84)	117.1 ± 1.6	9.03 ± 1.00	0.077 ± 0.010	2.85 ± 0.01	−0.731 [−0.168]
C_6	0.391 (16.53)	108.1 ± 2.5	3.90 ± 0.21	0.036 ± 0.003	2.82 ± 0.16	−0.789 [−0.157]
C_8	0.341 (18.78)	92.0 ± 4.5	2.01 ± 0.10	0.022 ± 0.002	2.76 ± 0.25	−0.728 [−0.127]
PEA	0.390 (16.41)	101.0 ± 2.2	10.5 ± 0.4	0.104 ± 0.007	2.96 ± 0.13	−0.836 [−0.186]

[a]Definitions are given in the main text or in Methods.

DOI: 10.1021/acsnano.9b05504
ACS Nano 2019, 13, 10745–10753

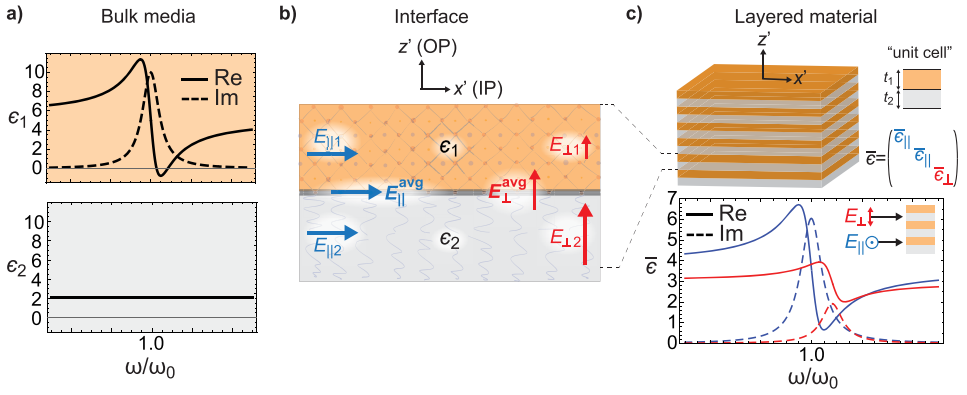

Figure 3. Origin of large effective optical uniaxiality in layered nanomaterials. (a) Permittivities of two hypothetical isotropic dielectric media. "Medium 1" (top; orange) shows a strong Lorentzian resonance at a frequency ω_0. "Medium 2" (bottom; gray) is completely transparent ($\mathrm{Im}(\epsilon_2) = 0$) and thus exhibits negligible dispersion. (b) Electric field matching conditions at the level of a single dielectric interface. The in-plane electric field (blue) is continuous across the interface. The out-of-plane electric field (red) exhibits a discontinuity because of the dielectric contrast and is suppressed in the high-permittivity medium. (c) A layered system is thus optically uniaxial even when the material constituents are isotropic. The calculated permittivities in (c) assume a fill factor, f_1, of 0.5 (*i.e.*, $t_1/(t_1 + t_2) = 0.5$).

subject to a harmonic electric field of frequency ω, $\vec{E}(x, y, z; \omega)$, is expressed as[42]

$$\Gamma_{fi} \propto |\underbrace{\vec{M}_{fi}}_{\substack{\text{quantum}\\ \text{mechanical}}} \cdot \underbrace{\vec{E}(x, y, z; \omega)}_{\text{classical}}|^2 \tag{1}$$

In the quantum-mechanical picture, $\vec{M}_{fi}$ is the transition dipole moment between states $|i\rangle$ and $|f\rangle$. That is, the rate of energy exchange to/from the electromagnetic field depends on the value of the *local* electric field (*i.e.*, $\vec{E}(x, y, z; \omega)$), which is, in turn, governed by the dielectric environment.[28,42,46,47] This distinction is critical for comparison with quantum-mechanical calculations.

We quantify this effect in 2D HOIPs by considering two distinct (hypothetical) linear and isotropic media (Figure 3a): "medium 1" (orange; top panel) and "medium 2" (gray; bottom pannel), with frequency-dependent relative permittivities, $\epsilon_1(\omega)$ and $\epsilon_2(\omega)$. "Medium 1"—an "active" material—shows a strong Lorentzian resonance at a frequency ω_0 (which may represent, for example, an exciton) with $\epsilon_1 < 0$ behavior over a small domain on the high-frequency side of the resonance. In stark contrast, "medium 2"—a "passive" material—has a relatively small permittivity and is completely transparent over this range, thus exhibiting negligible dispersion. Medium 1 and 2 are reasonable models for, for example, the metal halide and organic spacer layers in 2D HOIPs, respectively.[33,34,43] At the interfaces (Figure 3b), the parallel-to-interface ($\parallel$) and perpendicular-to-interface ($\perp$) electric field matching conditions are distinct; $E_\parallel$ (blue) is continuous across the interface, while $E_\perp$ (red) exhibits a sharp discontinuity according to (Supporting Information S4)

$$E_\parallel(z' = 0^-) = E_\parallel(z' = 0^+),$$
$$\epsilon_1 E_\perp(z' = 0^-) = \epsilon_2 E_\perp(z' = 0^+) \tag{2}$$

A material composed of many such alternating layers (Figure 3c; top panel) can be structurally described by the volumetric fill fraction of medium 1: $f_1 = t_1/(t_1 + t_2)$, where t_i ($i = 1, 2$) is the layer thickness of medium i. If the alternating layers are each much thinner than the optical wavelength, the composite material can be optically described with *effective* parallel ($\bar{\epsilon}_\parallel$) and perpendicular ($\bar{\epsilon}_\perp$) permittivities according to basic constitutive relations.[48] Given the differences expressed in eq 2, the *effective* parallel and perpendicular optical constants represent different averages. Generalizing eq 2 to account for *intrinsically* uniaxial constituents, each with permittivity tensors $\epsilon_i = \mathrm{diag}(\epsilon_{i,\parallel}, \epsilon_{i,\parallel}, \epsilon_{i,\perp})$ ($i = 1, 2$), we arrive at (Supporting Information S4)

$$\bar{\epsilon}_\parallel = f_1\epsilon_{1,\parallel} + (1 - f_1)\epsilon_{2,\parallel}, \quad \bar{\epsilon}_\perp = \frac{1}{f_1/\epsilon_{1,\perp} + (1 - f_1)/\epsilon_{2,\perp}} \tag{3}$$

At this level of description, the layered material is now effectively homogeneous, but uniaxial with an *effective* permittivity tensor $\bar{\epsilon} = \mathrm{diag}(\bar{\epsilon}_\parallel, \bar{\epsilon}_\parallel, \bar{\epsilon}_\perp)$.[48] Figure 3c (bottom panel) shows the *effective* IP (blue) and OP (red) permittivities calculated for our hypothetical layered medum with $f_1 = 0.5$. This crystal exhibits a uniaxial optical response markedly different from that of either bulk constituent. The IP optical response is reduced slightly due to volumetric averaging between active and passive layers. More noticeably, the OP optical response is reduced significantly due to suppression of the local perpendicular electric field, $E_\perp$ (eq 2), within the absorbing regions due to their relatively high local permittivity. Although the absorbing medium is isotropic at an *intrinsic* level, the layered medium acquires a significantly anisotropic *effective* optical response.

Optical experiments invariably measure the *effective* optical properties of layered HOIPs. Using the effective-medium model (EMM) described above, however, we can gain a better understanding of the *intrinsic* optical properties. For instance, the decrease in $\mathrm{Im}(\bar{\epsilon}_\parallel)$ can be predicted from a decrease in the volumetric fill fraction of PbI layers (f_{PbI}) (Figure S8). Similarly, large measured anisotropies arise from field inhomogeneities described in eq 2. To facilitate comparison between experiment and quantum-mechanical calculations, we exploit eq 3 to extract the *intrinsic* optical constants, $\epsilon_\parallel^{\mathrm{int}}$ and $\epsilon_\perp^{\mathrm{int}}$, from measured optical constants, $\bar{\epsilon}_\parallel$ and $\bar{\epsilon}_\perp$. Namely, we equate the right-hand side of the EMM expressions (eq 3) to the measured optical constants, input known structural parameters, and solve for the intrinsic optical constants of the PbI monolayers (Methods). Because of the vertically layered thin-film structure of R_2PbI_4, equations relating IP ($\parallel$) and OP ($\perp$) expressions can be solved independently.

DOI: 10.1021/acsnano.9b05504
ACS Nano 2019, 13, 10745−10753

Exemplary *intrinsic* PbI optical constants resulting from this calculation are presented in Figure S9. The results indicate an *intrinsic* OP:IP absorption strength ratio of approximately 0.3, as compared to 0.08 inferred from thin films directly. That is, anisotropies in the quantum-mechanical matrix elements reduce the OP dipole strength by only a factor of ∼1/3; in contrast, classical electric field inhomogeneities play a larger role, leading to a further reduction by a factor of ∼1/4 and even larger factors in films prepared with longer organic cations. This suggests the simple route to tuning significantly the macroscopic optical anisotropies, *i.e.*, by varying the length and polarizability of the organic cation. The corrected $(C_4)_2PbI_4$ high-frequency OP permittivity ($\epsilon^{int}_{\perp,\infty} \approx 4.1$ for $\lambda > 1000$ nm; Figure S9) can now be compared directly to calculations in refs 33 and 34, and both are found to be in very good agreement. The high-frequency IP permittivity ($\epsilon^{int}_{\parallel,\infty} \approx 4.7$) is most easily compared to the 3D system $(C_1)PbI_3$. Although the IP bonding structure of R_2PbI_4 is similar to that of $(C_1)PbI_3$, atomic-scale continuity with neighboring low-permittivity organic layers should suppress the dielectric constant relative to bulk values. We thus conclude that the EMM as developed here accurately described the relationship between experimentally observed (*i.e.*, effective) and theoretically predicted (*i.e.*, intrinsic) optical anisotropies.

Although eqs 2 and 3 hold independently at each wavelength, we simplify subsequent analyses by deriving (for each material) a single wavelength-averaged correction factor that accounts for the EMM effects (Supporting Information S5). The relations are particularly simple for the vertically layered thin-film structure of R_2PbI_4; the OP dipole strength ($|M_{OP}|^2$) correction depends on the dielectric contrast and (implicitly) the volumetric fill fraction of PbI layers:

$$|M^{int}_{OP}|^2 = \langle |\epsilon^{int}_{\perp}/\bar{\epsilon}_{\perp}|^2 \rangle \times |M_{OP}|^2 \quad (4)$$

in which $\langle\rangle$ denotes spectral averaging over the absorption (or emission) band (Methods). As before, $\bar{\epsilon}_{\perp}$ is the *effective* OP permittivity of the crystal. Note that $\epsilon^{int}_{\parallel,\perp}$ corresponds to the material in which the absorption or emission process is localized (*e.g.*, the PbI layers in 2D HOIPs). To evaluate these correction factors, the dielectric and structural properties of the material constituents must be known. To this end, we use $\epsilon^{int}_{\parallel,\perp}$ derived from the procedures described in the previous section (Figure S9).

Figure 4 summarizes absorption (left panel) and emission (right panel) anisotropies inferred directly from thin-film measurements ("effective"; orange markers) and after applying EMM corrections ("intrinsic"; purple markers) for all of the materials studied here. The inferred anisotropies in the PbI layers are uniformly smaller than in the homogeneous layered medium. Notably, after accounting for variations in length and permittivities of the organic layers, we find a similar degree of absorption anisotropy (OP:IP ≈ 0.3) between films prepared with C_4, C_6, and PEA. Films prepared with C_8 still show a relatively small OP:IP ratio (≈0.12) after this correction, which likely results from experimental errors, particularly in the OP optical constants. Since emission and absorption correction factors are (nearly) equivalent, relatively small *effective* OP:IP ratios lead to correspondingly small *corrected* ratios. Interestingly, residual variations are found in emission ratios but are absent in absorption ratios. Some portion of this discrepancy may arise from compounded experimental uncertainties; the inferred OP dipole strengths are particularly sensitive to the input optical constants. The results also depend upon the assumed distribution of emitter positions within the film (Methods). However, to what degree this discrepancy arises from experimental artifacts or inherent differences in optical processes remains unresolved at the current time. For comparison, we also include values from ref 35 (down triangles) before and after applying corrections derived here. (Note that ref 35 quotes OP percentages; here we have converted to OP:IP ratios.) Although absolute values differ between that work and ours, the trend between materials agrees well. We suspect ratios derived in ref 35 are overestimated since effective values are significantly larger than those inferred here and in ref 6 and since corrected values are very large (exceeding 1 in the case of $m = 4$).

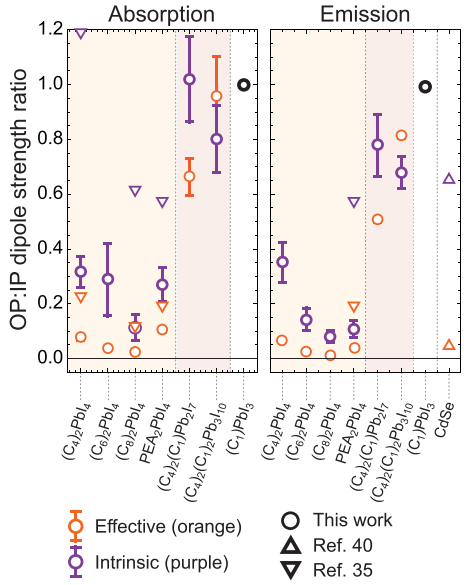

Figure 4. Summary of effective *vs* intrinsic anisotropies in layered nanomaterials. Orange markers: *Effective* OP:IP ratios for various materials determined in (circles) this work, (up triangles) ref 40, and (down triangles) ref 35. Purple markers: *Intrinsic* OP:IP ratios calculated by techniques described in the main text. Error bars represent estimates of 99% confidence intervals, primarily originating from uncertainties in optical constants. Absence of error bars indicates no confidence estimate or confidence intervals approximately equivalent to marker sizes.

Leveraging this analysis, we can now quantify and understand optical anisotropies in films of butylammonium methylammonium lead iodide, $(C_4)_2(C_1)_{N-1}Pb_NI_{3N+1}$, with $N > 1$, which tend to consist of statistical mixtures of oriented crystallites (Supporting Information S5).[49,50] The corrections described in eq 4 can be extended to account for this crystallite reorientation (Supporting Information S4 and S5). Similar EMM treatments have successfully been applied to quantify the role of anisotropic intrinsic carrier mobilities in ensembles of conducting oxide nanocrystals.[51] Interestingly, for both $N = 2$ and $N = 3$ HOIPs, we find nearly isotropic absorption and emission (Figure S10) after accounting for EMM effects, which likely reflects "new" Pb and I p_z orbital contributions in the bonding structure that are highly suppressed in the limit of the monolayer system.[38,52] We note, however, that phase intergrowth in the thin-film structure for $N > 1$ may reduce the applicability of the model derived here.[50]

DOI: 10.1021/acsnano.9b05504
ACS Nano 2019, 13, 10745−10753

CONCLUSIONS

The EMM derived here can be immediately applied to other material systems with layered geometries. For example, we consider previous mPL analyses of CdSe nanoplatelets as studied by Scott *et al.*[40] In that work, monolayers of highly oriented CdSe nanoplatelets were immersed in an oleic acid matrix and deposited on transparent substrates. As per typical mPL analyses, radiation patterns were modeled using a three-layer Fresnel model with *effective* (*i.e.*, homogeneous and uniaxial) optical constants (see Supplementary Tables I and II of ref 40). Within that model, observed radiation patterns correspond to an *effective* OP contribution of 5% (OP:IP ratio of 0.052) (Figure 4, orange up triangle). However, at a more rigorous level, these radiation patterns arise from a five-layer system (Figure S11). This is indeed an analytically tractable problem, using the same formalism as presented in previous reports,[28,40,47] but extended using electric fields calculated for a five-layer model.[53] These calculations (Figure S11) reveal that radiation patterns observed in ref 40 correspond to an *intrinsic* OP contribution of 41% (OP:IP ratio of ≈0.66) (Figure 4, purple up triangle), an order of magnitude larger than that inferred by Scott *et al.*[40] This discrepancy is captured very well using the simple correction factors described above ($|\epsilon_{\perp}^{\mathrm{int}}/\bar{\epsilon}_{\perp}|^2 = |(7.9 + i2.6)/(2.332 + i0.026)|^2 \approx 12.7$), further validating the simplified procedure described in this work. Indeed, this corrected ratio is more compatible with emission anisotropies observed in III−V quantum-well systems,[54,55] in which the effects of dielectric inhomogeneity are minimized, and in other CdSe nanoplatelet[56] and nanowire studies.[57]

Knowledge of the *effective* optical properties is suitable for understanding, for example, angle-dependent reflection, transmission, and absorption rates. The optical constants reported here will thus be useful for modeling and optimizing 2D HOIP-based optoelectronic devices. These macroscopic optical properties, however, do *not* directly reflect the properties of the material constituents; classical corrections must be applied before attributing the optical properties to the underlying electronic structure and anisotropies in the quantum-mechanical transition dipole moment. We show how these differences can be simply accounted for using correction factors derived from an effective-medium model. In particular, in OP-layered nanomaterials, quantum-mechanical OP dipole moments are substantially underestimated—by a factor of approximately 5 or greater in 2D HOIPs—when ignoring dielectric inhomogeneties. In the most significant case considered here (CdSe nanoplatelets), we have shown that inferred quantum-mechanical anisotropies were overestimated by approximately a factor of 10. After accounting for such effects, absorption anisotropies in 2D HOIPs are found nearly independent of the choice of the *R* cation. This study illustrates how experimentally inferred optical anisotropies relate to quantum-mechanical calculations in any material and offers an intuitive explanation for previously unexplained variations in optical properties of 2D HOIPs. Our model may also provide guidelines for predicting and designing birefringence properties in layered compounds.

METHODS

Samples. Solutions of $(C_m)_2PbI_4$ (m = 4, 6, 8) and PEA_2PbI_4 were prepared by dissolving stoichiometric ratios of *n*-butylammonium iodide (m = 4), *n*-hexylammonium iodide (m = 6), *n*-octylammonium iodide (m = 8), or phenethylammonium iodide (Greatcell Solar Materials) with lead(II) iodide (PbI_2) (TCI America) in anhydrous *N*,*N*-dimethylformamide (DMF) to concentrations of 1 M [Pb]. These "mother" solutions were then diluted to approximately 0.2 and 0.07 M in DMF. Solutions of $(C_4)_2(C_1)_{N-1}Pb_NI_{3N+1}$(butylammonium methylammonium lead iodide), with N = 2, 3, and solutions of C_1PbI_3 (methylammonium lead iodide) were prepared similarly, to concentrations of 150 and 200 mg/mL, respectively. For mR and mPL measurements of $C_mH_{2m+1}NH_3PbI_4$ (m = 4, 6, 8), thin films were prepared on 0.180 mm fused silica substrates (SPI Supplies) from 0.07 mol/mL solutions by dropping and subsequent spinning at 2k rpm (m = 4, m = 8, and PEA films) and 1500 rpm (C_6 films) for 60 s. Speeds were chosen to yield films with equivalent thicknesses, up to experimental accuracy limited by imaging resolution of atomic force microscopy and thin-film surface texture. For ellipsometry measurements, m = 4, 6, 8, and PEA films were prepared on Si wafers (⟨100⟩, single-side polish, native oxide, 1−10 Ωcm) (iWS) from 0.2 mol/mL solutions by dropping and subsequent spinning at 8k rpm (m = 4, 6 and PEA films) and 6k rpm (m = 8 films) for 60 s. Films were thermally annealed at 100 °C for 10 min. Thin films of $(C_4)_2(C_1)_{N-1}Pb_NI_{3N+1}$were prepared on 0.180 mm fused silica substrates and Si wafers by spinning at 8k rpm for 60 s and were subsequently thermally annealed at 100 °C for 30 min. Film thicknesses were measured with atomic force microscopy (AFM) (Asylum MFP-3D) in tapping mode by using a tip-scratch method and scanning over the resulting groove. Surface RMS for each sample was measured with AFM in tapping mode by scanning untouched surfaces. Phase purity and structural information were determined by X-ray diffraction (XRD) measurements (Malvern Panalytical Empyrian). mR and mPL measurements were performed under a heavy flow of N_2 gas. Ellipsometry and XRD were performed in ambient conditions. All solutions and samples were prepared in a nitrogen-vacated glovebox until the time of measurement.

Experimental Setup. All energy-momentum spectroscopies (mR and mPL) were performed with a Nikon Eclipse Ti−U inverted microscope with a 1.3 NA oil-immersion objective (Nikon CFI Plan Fluor 100XS) using a setup similar to the one used in refs 47 and 28. The energy and $\hat{y}$-momentum distribution of reflection/PL were measured by imaging the objective's BFP to the entrance slit of an imaging spectrometer (Princeton Instruments IsoPlane SCT-320) equipped with a CCD array (Princeton Instruments Pixis 1024BRX). An analyzing linear polarizer was applied such that light along the k_y-axis was either p-polarized (y polarizer alignment) or s-polarized (x polarizer alignment). For mR, samples were illuminated with a nearly uniform distribution in k-space by illuminating diffuser films (located at the objective's BFP at the rear port of the microscope) with polarized white light. This illuminates the samples with incident momenta ranging from normal incidence ($k_{\parallel} = 0$, $\theta = 0°$) to approximately $k_{\parallel}/k_0 = 1.3$ ($\theta \approx 64°$) from within the substrate, well beyond the critical angle of total internal reflection. Momentum-resolved specular reflectance was collected with the same objective. For mPL, samples were pumped at normal incidence in a reflection-model geometry using a 405 nm table-top fiber-coupled laser source (Thorlabs) loosely focused to a ≈100 μm spot at the level of the sample. Incident light was filtered by a 405 nm short-pass filter and reflected by a 415 nm dichroic mirror to remove overlap with the emission wavelengths. Collected PL was transmitted through the 405 nm dichroic and a 417 nm long-pass filter. Optical excitation energy densities were kept below ∼5 mW/cm^2. All measurements were performed under a generous flow of N_2 to minimize photoinduced degradation during exposures. Exposure times were on the order of 100 s.

Optical Constants. Complete details of the joint mR/VASE procedures are provided in the Supporting Information Sect. S2.

Calculating Oriented Electric Dipole Moments and "Strengths". In this work, we adopt the definition of dipole "moment", $|M_i(\omega)|$, and dipole "strength", $|M_i(\omega)|^2$, from ref 28: $|M_i(\omega)|^2 = \bar{n}_i|\mu_{\mathrm{ED},i}(\omega)|^2$, where $\bar{n}_i$ and $\mu_{\mathrm{ED},i}$ are the numbers and individual dipole moments, respectively, of $\hat{i}$-oriented dipoles. Normalized IP and OP absorption dipole strengths were determined by integrating $\mathrm{Im}(\epsilon_{\parallel})$ and $\mathrm{Im}(\epsilon_{\perp})$ over the exciton absorption band. In this case, $\epsilon_{\parallel}$ and $\epsilon_{\perp}$ were taken from parametrized optical constants

DOI: 10.1021/acsnano.9b05504
ACS Nano 2019, 13, 10745−10753

(*e.g.*, Figure 1d). IP and OP emission dipole moments and strengths were determined independently at each wavelength by fitting p-polarized mPL spectra to calculated radiation patterns.[28,29,31] The thin-film optical constants used in these calculations are presented in Figure 1 and Figure S3. Normalized IP and OP integrated emission dipole strengths were determined by integrating $|M_{IP/OP}(\omega)|^2$ over the emission band. Film thicknesses were taken to be the mean thicknesses as determined by AFM. (We find that using a symmetric distribution of thicknesses centered around the mean, as in the mR procedure described in Supporting Information Sect. S2, provided negligible changes in the results.) The emitting dipoles were assumed to be distributed uniformly at discrete positions along the *z*-axis within the film. The inferred dipole strengths will vary depending on the assumed distribution of emitters within the film. We chose the simplest distribution to minimize the number of input free parameters in our analysis.

Calculating Quantities Presented in Table 1. f_{PbI} was determined by dividing the thickness of PbI octahedra layers (assumed to be a constant 6.4 Å)[6,11] by the PbI interlayer spacing as determined from XRD. $\bar{\epsilon}_{\perp,\infty}$ was taken directly from ellipsometric Cauchy fits at 1000 nm. Δn at λ = 1000 nm was determined directly from ellipsometric Cauchy fits (Supporting Information S2). Δn at λ = 530 nm was determined from fully parametrized optical constants (*e.g.*, Figure 1c). We define 530 nm as the absorption onset based upon raw mR fit results (Figure S3).

Calculating Corrected Oscillator Strengths. For absorption in N = 1 materials, the intrinsic OP:IP ratio was derived by integrating $\epsilon_{\parallel,\perp}^{int}$ over the exciton absorption band. For all other calculations, dipole strength correction factors were derived according to eq 4 (for N = 1 materials) and eqs S32−S34 (for N > 1 materials). For simplicity, for each material, we define a single correction value based on the *average* values of $\bar{\epsilon}_\perp$ and $\epsilon_\perp^{int}$ around the exciton absorption (and emission) peak. This is reasonable in the case at hand due to the relatively small variations in $\bar{\epsilon}_\perp$ and, in the case of absorption, since the peak of the absorption band occurs approximately where $\mathrm{Re}(\epsilon_\perp)$ takes that average value. To calculate intrinsic optical constants (*e.g.*, Figure S9), we assume the refractive index of the organic layer is isotropic since precise estimates of anisotropies are not known. For C_m with m = 4, 6, and 8, we assume a refractive index of 1.5, 1.49, and 1.48, respectively, to account for the approach to more "bulk-like" refractive index as the width of the organic layers is increased. For PEA, we assume a refractive index of 1.6 to account for the increased polarizability of PEA as compared to C_m. Confidence intervals were estimated by calculating quantities using the maximum ($+3\sigma$) and minimum (-3σ) estimates for the optical constants (*e.g.*, Figure S3).

Modeling mPL from an Inhomogeneous CdSe Nanoplatelet System. Polarized radiation patterns were calculated using the formalism presented in refs 47, 28, and 40 extended to a five-layer system. Namely, using the reciprocity formalism, the emission rate of IP- and OP-oriented EDs is related to the IP and OP components of the local electric-field magnitude squared. The electric field magnitudes were calculated using transfer matrix methods detailed in ref 53. This problem is analytically tractable, but the resulting field expressions are not written out in this work because they are prohibitively long. All parameters used for this calculation are taken directly from ref 40. Specifically, we calculate p-polarized radiation patterns at 515 nm from a planar five-layer system consisting of the following layers: (1) fused silica substrate; (2) oleic acid; (3) CdSe; (4) oleic acid; (5) vacuum. Thicknesses, specified in Figure S11, are (1) semi-infinite, z < 0; (2) 2.1 nm; (3) 1.4 nm; (4) 2.1 nm; (5) semi-infinite, z > 5.6 nm. Relative (isotropic) permittivities are (1) 1.46^2 = 2.1316; (2) 2.129; (3) 7.9 + *i*2.6; (4) 2.129; (5) 1. An OP:IP ratio of 0.66 was taken for the best representation of the data. For the effective system, we use the standard three-layer formalism and assume relative (uniaxial) permittivities for the center layer as specified in Supplementary Table 2 of ref 40 (ϵ_{eff}^{IP} = 2.652 + *i*0.192; ϵ_{eff}^{OP} = 2.332 + *i*0.026). An OP:IP ratio of 0.05/0.95 = 1:19 was used, in accordance with the ratio inferred in ref 40.

ASSOCIATED CONTENT

Supporting Information

The Supporting Information is available free of charge on the ACS Publications website at DOI: 10.1021/acsnano.9b05504.

Supporting discussion, experimental details, theoretical details, and figures (PDF)

Tabulated optical constants of $(C_m)_2PbI_4$ m = 4 (TXT)

Tabulated intrinsic optical constants derived from $(C_m)_2PbI_4$ m = 4 (TXT)

Tabulated optical constants of $(C_m)_2PbI_4$ m = 6 (TXT)

Tabulated optical constants of $(C_m)_2PbI_4$ m = 8 (TXT)

Tabulated optical constants of PEA_2PbI_4 (TXT)

Tabulated optical constants of $(C_4)_2(C_1)_{N-1}Pb_NI_{3N+1}$ N = 2 (TXT)

Tabulated optical constants of $(C_4)_2(C_1)_{N-1}Pb_NI_{3N+1}$ N = 3 (TXT)

AUTHOR INFORMATION

Corresponding Author

*E-mail: jonschuller@ece.ucsb.edu.

ORCID

Ryan A. DeCrescent: 0000-0003-3219-7736

Naveen R. Venkatesan: 0000-0003-2086-5274

Clayton J. Dahlman: 0000-0002-4555-4846

Michael L. Chabinyc: 0000-0003-4641-3508

Jon A. Schuller: 0000-0001-6949-3569

Notes

The authors declare no competing financial interest.

ACKNOWLEDGMENTS

The authors thank Chris G. Van de Walle, Xie Zhang, Boubacar Traore, and André Schleife for helpful discussions. Materials synthesis and structural characterization were supported by the U.S. Department of Energy, Office of Science, Basic Energy Sciences, under Award Number DE-SC-0012541. Energy-momentum spectroscopy measurements and analyses were supported by the National Science Foundation (DMR-1454260 and OIA- 1538893) and by the Air Force Office of Scientific Research (Grant No. FA9550-16-1-0393). A portion of this work was performed in the UCSB Nanofabrication Facility. The research reported here also made use of the shared facilities of the UCSB MRSEC (National Science Foundation DMR 1720256), a member of the Materials Research Facilities Network (www.mrfn.org). R.M.K. gratefully acknowledges the National Defense Science and Engineering Graduate fellowship for financial support.

REFERENCES

(1) Song, X.; Hu, J.; Zeng, H. Two-Dimensional Semiconductors: Recent Progress and Future Perspectives. *J. Mater. Chem. C* **2013**, *1*, 2952−2969.

(2) Bernardi, M.; Ataca, C.; Palummo, M.; Grossman, J. C. Optical and Electronic Properties of Two-Dimensional Layered Materials. *Nanophotonics* **2017**, *6*, 479−493.

(3) Tian, H.; Tice, J.; Fei, R.; Tran, V.; Yan, X.; Yang, L.; Wang, H. Low-Symmetry Two-Dimensional Materials for Electronic and Photonic Applications. *Nano Today* **2016**, *11*, 763−777.

(4) Ponraj, J. S.; Xu, Z.-Q.; Dhanabalan, S. C.; Mu, H.; Wang, Y.; Yuan, J.; Li, P.; Thakur, S.; Ashrafi, M.; McCoubrey, K.; Zhang, Y.; LI, S.; Zhang, H.; Bao, Q. Photonics and Optoelectronics of Two-Dimensional Materials Beyond Graphene. *Nanotechnology* **2016**, *27*, 462001.

DOI: 10.1021/acsnano.9b05504
ACS Nano 2019, 13, 10745−10753

(5) Brar, V. W.; Sherrott, M. C.; Jariwala, D. Emerging Photonic Architectures in Two-Dimensional Opto-Electronics. *Chem. Soc. Rev.* **2018**, *47*, 6824−6844.
(6) Ishihara, T.; Takahashi, J.; Goto, T. Optical Properties Due to Electronic Transitions in Two-Dimensional Semiconductors $(C_nH_{2n+1}NH_3)_2PbI_4$. *Phys. Rev. B: Condens. Matter Mater. Phys.* **1990**, *42*, 11099−11107.
(7) Tanaka, K.; Kondo, T. Bandgap and Exciton Binding Energies in Lead-Iodide-Based Natural Quantum-Well Crystals. *Sci. Technol. Adv. Mater.* **2003**, *4*, 599−604.
(8) Pedesseau, L.; Sapori, D.; Traore, B.; Robles, R.; Fang, H.-H.; Loi, M. A.; Tsai, H.; Nie, W.; Blancon, J.-C.; Neukirch, A.; Tretiak, S.; Mohite, A. D.; Katan, C.; Even, J.; Kepenekian, M. Advances and Promises of Layered Halide Hybrid Perovskite Semiconductors. *ACS Nano* **2016**, *10*, 9776−9786.
(9) Katan, C.; Mercier, N.; Even, J. Quantum and Dielectric Confinement Effects in Lower-Dimensional Hybrid Perovskite Semiconductors. *Chem. Rev.* **2019**, *119*, 3140−3192.
(10) Billing, D. G.; Lemmerer, A. Synthesis, Characterization and Phase Transitions in the Inorganic-Organic Layered Perovskite-Type Hybrids $[(C_nH_{2n+1}NH_3)_2PbI_4]$, N = 4, 5 and 6. *Acta Crystallogr., Sect. B: Struct. Sci.* **2007**, *63*, 735−747.
(11) Stoumpos, C. C.; Cao, D. H.; Clark, D. J.; Young, J.; Rondinelli, J. M.; Jang, J. I.; Hupp, J. T.; Kanatzidis, M. G. Ruddlesden-Popper Hybrid Lead Iodide Perovskite 2D Homologous Semiconductors. *Chem. Mater.* **2016**, *28*, 2852−2867.
(12) Tsai, H.; Nie, W.; Blancon, J.-C.; Stoumpos, C. C.; Asadpour, R.; Harutyunyan, B.; Neukirch, A. J.; Verduzco, R.; Crochet, J. J.; Tretiak, S.; Pedesseau, L.; Even, J.; Alam, M. A.; Gupta, G.; Lou, J.; Ajayan, P. M.; Bedzyk, M. J.; Kanatzidis, M. G.; Mohite, A. D. High-Efficiency Two-Dimensional Ruddlesden-Popper Perovskite Solar Cells. *Nature* **2016**, *536*, 312−316.
(13) Lédée, F.; Trippé-Allard, G.; Diab, H.; Audebert, P.; Garrot, D.; Lauret, J.-S.; Deleporte, E. Fast Growth of Monocrystalline Thin Films of 2D Layered Hybrid Perovskite. *CrystEngComm* **2017**, *19*, 2598−2602.
(14) Fujita, T.; Sato, Y.; Kuitani, T.; Ishihara, T. Tunable Polariton Absorption of Distributed Feedback Microcavities at Room Temperature. *Phys. Rev. B: Condens. Matter Mater. Phys.* **1998**, *57*, 12428−12434.
(15) Lanty, G.; Bréhier, A.; Parashkov, R.; Lauret, J. S.; Deleporte, E. Strong Exciton-Photon Coupling at Room Temperature in Microcavities Containing Two-Dimensional Layered Perovskite Compounds. *New J. Phys.* **2008**, *10*, 065007.
(16) Yaffe, O.; Chernikov, A.; Norman, Z. M.; Zhong, Y.; Velauthapillai, A.; Van der Zande, A.; Owen, J. S.; Heinz, T. F. Excitons in Ultrathin Organic-Inorganic Perovskite Crystals. *Phys. Rev. B: Condens. Matter Mater. Phys.* **2015**, *92*, 045414.
(17) Dou, L.; Wong, A. B.; Yu, Y.; Lai, M.; Kornienko, N.; Eaton, S. W.; Fu, A.; Bischak, C. G.; Ma, J.; Ding, T.; Ginsberg, N. S.; Wang, L.-W.; Alivisatos, A. P.; Yang, P. Atomically Thin Two-Dimensional Organic-Inorganic Hybrid Perovskites. *Science* **2015**, *349*, 1518−1521.
(18) Cao, D. H.; Stoumpos, C. C.; Farha, O. K.; Hupp, J. T.; Kanatzidis, M. G. 2D Homologous Perovskites as Light-Absorbing Materials for Solar Cell Applications. *J. Am. Chem. Soc.* **2015**, *137*, 7843−7850.
(19) Tsai, H.; Nie, W.; Blancon, J.-C.; Stoumpos, C. C.; Soe, C. M. M.; Yoo, J.; Crochet, J.; Tretiak, S.; Even, J.; Sadhanala, A.; Azzellino, G.; Brenes, R.; Ajayan, P. M.; Bulović, V.; Stranks, S. D.; Friend, R. H.; Kanatzidis, M. G.; Mohite, A. D. Stable Light-Emitting Diodes Using Phase-Pure Ruddlesden-Popper Layered Perovskites. *Adv. Mater.* **2018**, *30*, 1704217.
(20) Yang, R.; Li, R.; Cao, Y.; Wei, Y.; Miao, Y.; Tan, W. L.; Jiao, X.; Chen, H.; Zhang, L.; Chen, Q.; Zhang, H.; Zou, W.; Wang, Y.; Yang, M.; Yi, C.; Wang, N.; Gao, F.; Mcneill, C. R.; Qin, T.; Wang, J.; et al. Oriented Quasi-2D Perovskites for High Performance Optoelectronic Devices. *Adv. Mater.* **2018**, *30*, 1804771.
(21) Raghavan, C. M.; Chen, T.-P.; Li, S.-S.; Chen, W.-L.; Lo, C.-Y.; Liao, Y.-M.; Haider, G.; Lin, C.-C.; Chen, C.-C.; Sankar, R.; Chang, Y.-M.; Chou, F.-C.; Chen, C.-W. Low-Threshold Lasing from 2D Homologous Organic-Inorganic Hybrid Ruddlesden-Popper Perovskite Single Crystals. *Nano Lett.* **2018**, *18*, 3221−3228.
(22) Zhang, L.; Liu, Y.; Yang, Z.; Liu, S. Two Dimensional Metal Halide Perovskites: Promising Candidates for Light-Emitting Diodes. *J. Energy Chem.* **2019**, *37*, 97−110.
(23) Woollam, J. A.; Johs, B. D.; Herzinger, C. M.; Hilfiker, J. N.; Synowicki, R. A.; Bungay, C. L. Overview of Variable-Angle Spectroscopic Ellipsometry (VASE): I. Basic Theory and Typical Applications. *Proceedings of Optical Metrology: A Critical Review*; SPIE, 1999; p 1029402.
(24) Hilfiker, J. N.; Singh, N.; Tiwald, T.; Convey, D.; Smith, S. M.; Baker, J. H.; Tompkins, H. G. Survey of Methods to Characterize Thin Absorbing Films with Spectroscopic Ellipsometry. *Thin Solid Films* **2008**, *516*, 7979−7989.
(25) Bu-Abbud, G. H.; Bashara, N. M. Parameter Correlation and Precision in Multiple-Angle Ellipsometry. *Appl. Opt.* **1981**, *20*, 3020−3026.
(26) Campoy-Quiles, M.; Etchegoin, P. G.; Bradley, D. D. C. On the Optical Anisotropy of Conjugated Polymer Thin Films. *Phys. Rev. B: Condens. Matter Mater. Phys.* **2005**, *72*, 045209.
(27) Campoy-Quiles, M.; Alonso, M. I.; Bradley, D. D. C.; Richter, L. J. Advanced Ellipsometric Characterization of Conjugated Polymer Films. *Adv. Funct. Mater.* **2014**, *24*, 2116−2134.
(28) Schuller, J. A.; Karaveli, S.; Schiros, T.; He, K.; Yang, S.; Kymissis, I.; Shan, J.; Zia, R. Orientation of Luminescent Excitons in Layered Nanomaterials. *Nat. Nanotechnol.* **2013**, *8*, 271−276.
(29) Brown, S. J.; Schlitz, R. A.; Chabinyc, M. L.; Schuller, J. A. Morphology-Dependent Optical Anisotropies in the N-Type Polymer P(NDI2OD-T2). *Phys. Rev. B: Condens. Matter Mater. Phys.* **2016**, *94*, 165105.
(30) DeCrescent, R. A.; Brown, S. J.; Schlitz, R. A.; Chabinyc, M. L.; Schuller, J. A. Model-Blind Characterization of Thin-Film Optical Constants with Momentum-Resolved Reflectometry. *Opt. Express* **2016**, *24*, 28842−28857.
(31) Brown, S. J.; DeCrescent, R. A.; Nakazono, D. M.; Willenson, S. H.; Ran, N. A.; Liu, X.; Bazan, G. C.; Nguyen, T.-Q.; Schuller, J. A. Enhancing Organic Semiconductor-Surface Plasmon Polariton Coupling with Molecular Orientation. *Nano Lett.* **2017**, *17*, 6151−6156.
(32) Dong, J.; Lu, R. Characterization of Weakly Absorbing Thin Films by Multiple Linear Regression Analysis of Absolute Unwrapped Phase in Angle-Resolved Spectral Reflectometry. *Opt. Express* **2018**, *26*, 12291−12305.
(33) Sapori, D.; Kepenekian, M.; Pedesseau, L.; Katan, C.; Even, J. Quantum Confinement and Dielectric Profiles of Colloidal Nanoplatelets of Halide Inorganic and Hybrid Organic-Inorganic Perovskites. *Nanoscale* **2016**, *8*, 6369−6378.
(34) Traore, B.; Pedesseau, L.; Assam, L.; Che, X.; Blancon, J.-C.; Tsai, H.; Nie, W.; Stoumpos, C. C.; Kanatzidis, M. G.; Tretiak, S.; Mohite, A. D.; Even, J.; Kepenekian, M.; Katan, C. Composite Nature of Layered Hybrid Perovskites: Assessment on Quantum and Dielectric Confinements and Band Alignment. *ACS Nano* **2018**, *12*, 3321−3332.
(35) Fieramosca, A.; De Marco, L.; Passoni, M.; Polimeno, L.; Rizzo, A.; Rosa, B. L. T.; Cruciani, G.; Dominici, L.; De Giorgi, M.; Gigli, G.; Andreani, L. C.; Gerace, D.; Ballarini, D.; Sanvitto, D. Tunable Out-of-Plane Excitons in 2D Single-Crystal Perovskites. *ACS Photonics* **2018**, *5*, 4179−4185.
(36) Ishihara, T.; Takahashi, J.; Goto, T. Exciton State in Two-Dimensional Perovskite Semiconductor $(C_{10}H_{21}NH_3)_2PbI_4$. *Solid State Commun.* **1989**, *69*, 933−936.
(37) Tanaka, K.; Sano, F.; Takahashi, T.; Kondo, T.; Ito, R.; Ema, K. Two-Dimensional Wannier Excitons in a Layered-Perovskite-Type Crystal $(C_6H_{13}NH_3)_2PbI_4$. *Solid State Commun.* **2002**, *122*, 249−252.
(38) Even, J.; Pedesseau, L.; Kepenekian, M. Electronic Surface States and Dielectric Self-Energy Profiles in Colloidal Nanoscale Platelets of CdSe. *Phys. Chem. Chem. Phys.* **2014**, *16*, 25182−25190.

DOI: 10.1021/acsnano.9b05504
ACS Nano 2019, 13, 10745−10753

(39) Lieb, M. A.; Zavislan, J. M.; Novotny, L. Single-Molecule Orientations Determined by Direct Emission Pattern Imaging. *J. Opt. Soc. Am. B* **2004**, *21*, 1210−1215.
(40) Scott, R.; Heckmann, J.; Prudnikau, A. V.; Antanovich, A.; Mikhailov, A.; Owschimikow, N.; Artemyev, M.; Climente, J. I.; Woggon, U.; Grosse, N. B.; Achtstein, A. W. Directed Emission of CdSe Nanoplatelets Originating from Strongly Anisotropic 2D Electronic Structure. *Nat. Nanotechnol.* **2017**, *12*, 1155−1160.
(41) Kikuchi, K.; Takeoka, Y.; Rikukawa, M.; Sanui, K. Structure and Optical Properties of Lead Iodide Based Two-Dimensional Perovskite Compounds Containing Fluorophenethylamines. *Curr. Appl. Phys.* **2004**, *4*, 599−602.
(42) Bastard, G. *Wave Mechanics Applied to Semiconductor Heterostructures*; EDP Sciences, 1988.
(43) Guo, P.; Huang, W.; Stoumpos, C. C.; Mao, L.; Gong, J.; Zeng, L.; Diroll, B. T.; Xia, Y.; Ma, X.; Gosztola, D. J.; Xu, T.; Ketterson, J. B.; Bedzyk, M. J.; Facchetti, A.; Marks, T. J.; Kanatzidis, M. G.; Schaller, R. D. Hyperbolic Dispersion Arising from Anisotropic Excitons in Two-Dimensional Perovskites. *Phys. Rev. Lett.* **2018**, *121*, 127401.
(44) Agranovich, V. M.; Kravtsov, V. E. Notes on Crystal Optics of Superlattices. *Solid State Commun.* **1985**, *55*, 85−90.
(45) Poddubny, A.; Iorsh, I.; Belov, P.; Kivshar, Y. Hyperbolic Metamaterials. *Nat. Photonics* **2013**, *7*, 948−957.
(46) Thorne, A. *Spectrophysics*; Springer Netherlands, 1988.
(47) Taminiau, T. H.; Karaveli, S.; Van Hulst, N. F.; Zia, R. Quantifying the Magnetic Nature of Light Emission. *Nat. Commun.* **2012**, *3*, 979.
(48) El-Haija, A. J. A. Effective Medium Approximation for the Effective Optical Constants of a Bilayer and a Multilayer Structure Based on the Characteristic Matrix Technique. *J. Appl. Phys.* **2003**, *93*, 2590−2594.
(49) Venkatesan, N. R.; Labram, J. G.; Chabinyc, M. L. Charge-Carrier Dynamics and Crystalline Texture of Layered Ruddlesden-Popper Hybrid Lead Iodide Perovskite Thin Films. *ACS Energy Lett.* **2018**, *3*, 380−386.
(50) Venkatesan, N. R.; Kennard, R. M.; DeCrescent, R. A.; Nakayama, H.; Dahlman, C. J.; Perry, E. E.; Schuller, J. A.; Chabinyc, M. L. Phase Intergrowth and Structural Defects in Organic Metal Halide Ruddlesden-Popper Thin Films. *Chem. Mater.* **2018**, *30*, 8615−8623.
(51) Dahlman, C. J.; Agrawal, A.; Staller, C. M.; Adair, J.; Milliron, D. J. Anisotropic Origins of Localized Surface Plasmon Resonance in N-Type Anatase TiO_2 Nanocrystals. *Chem. Mater.* **2019**, *31*, 502−511.
(52) DeCrescent, R. A.; Venkatesan, N. R.; Dahlman, C. J.; Kennard, R. M.; Zhang, X.; Li, W.; Chabinyc, M. L.; Zia, R.; Schuller, J. A. Bright Magnetic Dipole Radiation from Two-Dimensional Lead-Halide Perovskites. *Arxiv:1901.05136 [Cond-Mat]* **2019**, Arxiv: 1901.05136.
(53) Azzam, R.; Bashara, N. *Ellipsometry and Polarized Light*; North-Holland Personal Library; North-Holland Pub. Co., 1977.
(54) Aleshkin, v. Y.; Zvonkov, B. N.; Malkina, I. G.; Saf'yanov, Y. N.; Chernov, A. L.; Filatov, D. O. Polarization of In-Plane Photoluminescence from InAs/Ga(In)As Quantum-Well Layers Grown by Metallorganic Vapor-Phase Epitaxy. *Semiconductors* **1998**, *32*, 1119−1124.
(55) Masui, H.; Yamada, H.; Iso, K.; Nakamura, S.; DenBaars, S. P. Optical Polarization Characteristics of M-Oriented InGaN/GaN Light-Emitting Diodes with Various Indium Compositions in Single-Quantum-Well Structure. *J. Phys. D: Appl. Phys.* **2008**, *41*, 225104.
(56) Yoon, D.-E.; Kim, W. D.; Kim, D.; Lee, D.; Koh, S.; Bae, W. K.; Lee, D. C. Origin of Shape-Dependent Fluorescence Polarization from CdSe Nanoplatelets. *J. Phys. Chem. C* **2017**, *121*, 24837−24844.
(57) Hu, J.; Li, L.-S.; Yang, W.; Manna, L.; Wang, L.-W.; Alivisatos, A. P. Linearly Polarized Emission from Colloidal Semiconductor Quantum Rods. *Science* **2001**, *292*, 2060−2063.

DOI: 10.1021/acsnano.9b05504
ACS Nano 2019, 13, 10745−10753